Direct Observation of Conversion Between Threshold Switching and Memory Switching Induced by Conductive Filament Morphology

Haitao Sun, Qi Liu, Congfei Li, Shibing Long, Hangbing Lv, Chong Bi, Zongliang Huo, Ling Li, and Ming Liu**

Volatile threshold switching (TS) and non-volatile memory switching (MS) are two typical resistive switching (RS) phenomena in oxides, which could form the basis for memory, analog circuits, and neuromorphic applications. Interestingly, TS and MS can be coexistent and converted in a single device under the suitable external excitation. However, the origin of the transition from TS to MS is still unclear due to the lack of direct experimental evidence. Here, conversion between TS and MS induced by conductive filament (CF) morphology in Ag/SiO_2/Pt device is directly observed using scanning electron microscopy and high-resolution transmission electron microscopy. The MS mechanism is related to the formation and dissolution of CF consisting of continuous Ag nanocrystals. The TS originates from discontinuous CF with isolated Ag nanocrystals. The results of current–voltage fitting and Kelvin probe force microscopy further indicate that the TS mechanism is related to the modulation of the tunneling barrier between Ag nanocrystals in CF. This work provides clearly experimental evidence to deepen understanding of the mechanism for RS in oxide-electrolyte-based resistive switching memory, contributing to better control of the two RS behaviors to establish high-performance emerging devices.

1. Introduction

Resistive switching (RS) phenomenon induced by redox in oxide electrolyte provides attractive prospects for resistive random access memory (RRAM), analog circuits and other neuromorphic applications.[1–5] Due to simple structure, high speed, low power and excellent scalability, the redox-based RRAM is very suitable for 3D ultrahigh density storage.[6–12] Under external electrical stimulations, the resistance of the RRAM cell can be switched between high resistive state (HRS) and low resistive state (LRS) due to the formation/dissolution of conductive filament (CF) inside the insulator layer.[13–22] Although the kinetics of CF formation/dissolution is still unclear, it is widely accepted that the CF formation/dissolution is strongly related to the electromigration and electrochemical reaction of anion (i.e., oxygen vacancy)[13–16] or cation (i.e., Cu^{2+}, Ag^{+} or Ni^{2+}).[17–22]

Generally, RS behavior can be classified as two modes: nonvolatile memory switching (MS) and volatile threshold switching (TS). In the MS mode, both LRS and HRS can be maintained after removing the external voltage, while the LRS in the TS mode will be back to the HRS once the applied voltage is smaller than a critical value.[23–25] To avoid confusion with MS, the LRS and HRS in TS are renamed as "TS ON-state" and "TS OFF-state" in this article. The MS device can be used for the non-volatile data storage[1–5] while TS device can be as a selector in series with memory cell to suppress crosstalk effect in the crossbar array.[26–30] Recently, some groups reported that TS and MS can coexist and mutually transform in a single device at suitable external excitation.[23–28] Several models have been proposed to explain this phenomenon, including CF thermal instability,[23] strong electron correlation effect,[24] quantum-wire model,[25] interface barrier modulation,[26] and space charge effect.[27] However, the underlying mechanism of the phenomenon is still unclear, especially lacking of direct evidences to uncover when and how the two RS modes happen and what is the internal relationship between them.

Here, we demonstrate that the TS and MS modes can be modulated in the Ag/SiO_2/Pt structure by controlling the compliance current (I_{CC}) in electroforming. We systematically investigate the morphologies, chemical components, and dynamic growth of the CF using scanning electron microscope (SEM), high-resolution transmission electron microscopy (HRTEM) and electron energy loss spectroscopy (EELS) analysis. The results confirm that the TS and MS modes correspond to the CF consisting of isolated and continuous Ag nanocrystals, respectively. In addition, by Kelvin probe force microscopy (KPFM) studies, the voltage potential distribution of CF in the ON- and OFF-state further indicate that the TS mode is

H. Sun, Dr. Q. Liu, C. Li, Dr. S. Long, Dr. H. Lv, Dr. C. Bi, Prof. Z. Huo, Prof. L. Li, Prof. M. Liu
Lab of Nanofabrication and Novel Device Integration
Institute of Microelectronics
Chinese Academy of Sciences
Beijing 100029, China
E-mail: liuqi@ime.ac.cn; liuming@ime.ac.cn

DOI: 10.1002/adfm.201401304

dominated by the modulation of the tunneling barrier between discrete Ag nanocrystals.

2. Result and Discussion

Planar structure is often used to study the RS mechanism from the microscopic view due to easy observation on the change of CF between two electrodes.[21,31–33] In order to identify the dynamic process of CF in details and meanwhile ensure the electroforming operation successfully, an appropriate distance between Ag and Pt electrodes is needed. Hence, the gaps of $Ag/SiO_2/Pt$ planar device were designed from 100 nm to 2 μm. The schematic of device structure and typical SEM images of the device with different gap are illustrated in **Figure 1**a. The as-deposited devices are normally in the HRS and their initial resistances are more than 10^{11} Ω at 0.2 V read voltage. To trigger repeatable RS behavior in the fresh device, an electroforming process with positive voltage on Ag active electrode is required. TS or MS was observed in the $Ag/SiO_2/Pt$ device after electroforming with low or high I_{CC}, respectively, as shown in Figure 1b,c. During electroforming with I_{CC} = 100 nA, the current is quite small (below 10^{-11} A) with the increase of sweep voltage and suddenly increases to I_{CC} at a threshold voltage ($V_{th} \approx 20$ V). After the electroforming, another voltage sweep (0 V → 20 V → 0 V) with the same I_{CC} was applied. The initial current of this sweep is also ultra-low, indicating that the ON-state after electroforming was not maintained. When the voltage sweeps to a certain value (15 V), the current rapidly increases to I_{CC}. While when the voltage sweeps back to a certain value (5 V), the current decreases to the initial low level, implying a typical TS transition occurs (see the olive line in inset of Figure 1b). It is worth noting that when a negative voltage sweep (0 V → –20 V → 0 V) with same I_{CC} was applied on Ag electrode, a TS loop obviously symmetric to the positive one, as shown by the purple line in inset of Figure 1b. On the contrary, the device exhibits a MS characteristic when a high I_{CC} is applied to complete the electroforming (Figure 1c). After electroforming with I_{CC} = 100 μA, the device switches from HRS to LRS and the LRS can be maintained for a long time (>10^4 s at 85 °C, as shown in Supporting Information Figure S1a) after removing the voltage. Then, the device can be repeatably switched between LRS and HRS under the alternate negative RESET and positive SET operations (Figure 1c and Supporting Information Figure S1b). It is worth noting that the similar transition from TS to MS mode was also observed in the $Ag/SiO_2/Pt$ vertical device (Supporting Information Figure S2).

To reveal the underlying mechanism of the transition between TS and MS from the microscopic point of view, the morphology and chemical composition of the CFs formed in electroforming with different I_{CC} were analyzed in $Ag/SiO_2/Pt$ planar structure by SEM and HRTEM. **Figure 2**a shows that the gap between the two electrodes is clean in the as-deposited $Ag/SiO_2/Pt$ planar device. The devices respectively exhibit TS (Figure 2b,c) or MS (Figure 2d) modes after electroforming with low or high I_{CC}. Corresponding to the TS mode, SEM image

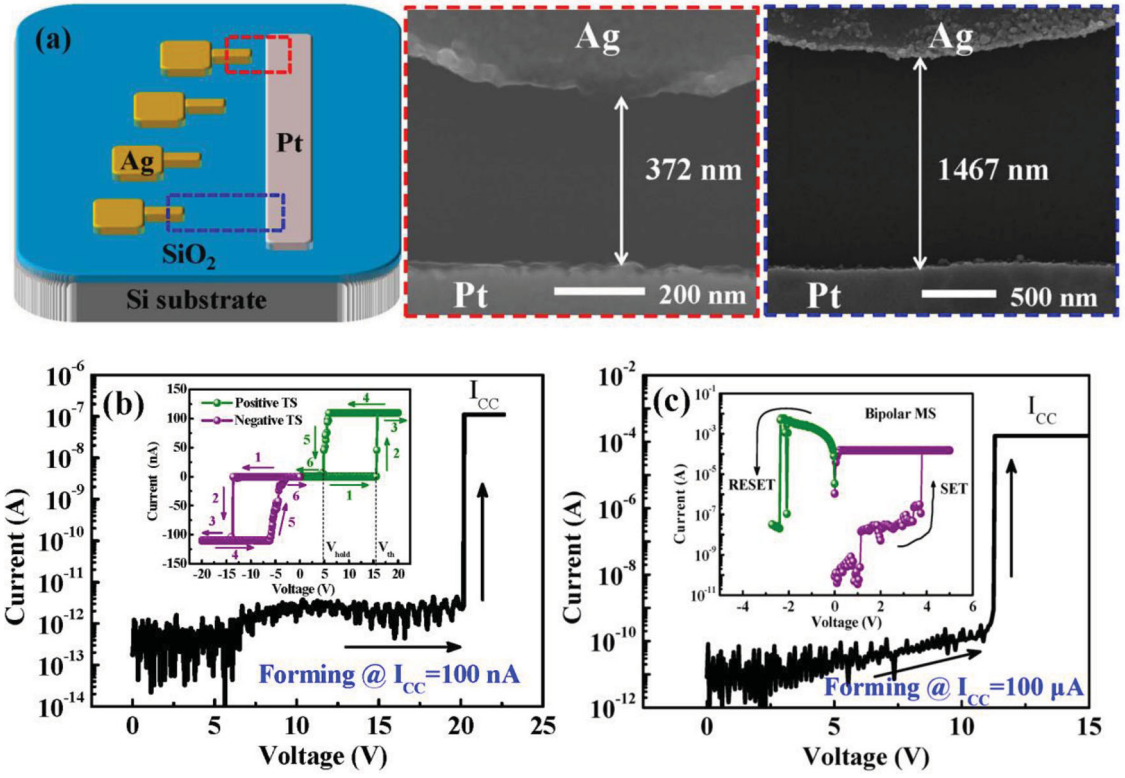

Figure 1. Device structure and electrical characteristics of the $Ag/SiO_2/Pt$. a) Schematic and SEM images of the planar device with various gap size. b) Current–voltage characteristics of electroforming process with I_{CC} = 100 nA. The inset is the symmetric TS behavior after low I_{CC} (100 nA) forming. c) Current–voltage characteristics of electroforming process with I_{CC} = 100 μA. The inset is the MS transition after relatively high I_{CC} (100 μA) forming.

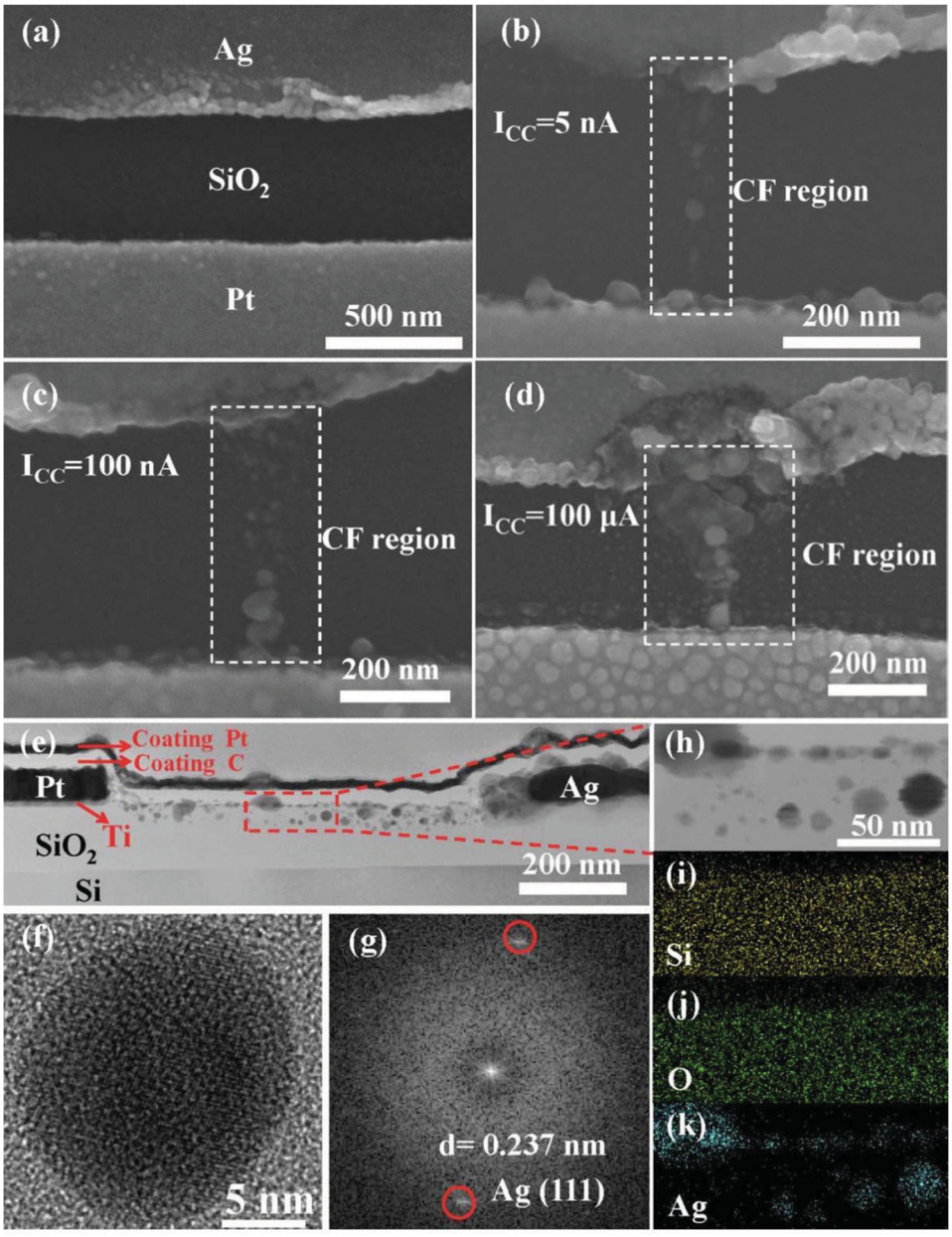

Figure 2. Morphology and component of CF observed in Ag/SiO_2/Pt planar structure after electroforming with various I_{CC}. a) As-prepared fresh device without any electrical treatment. b–d) Morphologies of the CF with I_{CC} = 5 nA, I_{CC} = 100 nA and I_{CC} = 100 μA, respectively. e) Cross-sectional TEM image along the nanocrystal chain. f) HRTEM images of a single nanoparticle. g) The diffraction pattern extracted by Fourier transform of (f) showing Ag (111) crystal plane. h) Enlarged TEM images taken from the red rectangular region in (e). i–k) EELS mapping images of Si, O and Ag elements, respectively, corresponding to the region in (h).

reveals that a CF consisting of some isolated nanoparticles is formed within the interelectrode region (Figure 2b,c). When the I_{CC} of electroforming is increased from 5 nA to 100 nA, the nanocrystal region widens and the space between the nanoparticles decreases (Figure 2b,c). When the I_{CC} is increased to 100 μA, these nanoparticles will further grow and connect with each other to form a continuous CF (Figure 2d), resulting in the MS mode.

Moreover, the microstructure and chemical component of the CF (nanoparticle chain) were investigated by HRTEM and EELS. The TEM sample was fabricated along the CF growth direction by a focused ion beam (FIB). Figure 2e shows the cross-sectional TEM image of the sample. As shown, the CF consists of some isolated nanoparticles distributing on the surface of and inside the bulk of SiO_2 layer. The nanoparticles have a sphere-like shape with dimensions in the range from several nanometers to several tens of nanometers. Figure 2f shows a typical HRTEM image of a single nanoparticle in CF. The clear lattice fringes and the corresponding fast Fourier transform (FFT) image (Figure 2g) indicate that the spherical nanoparticle

is highly crystalline. The measured fringes space is 0.237 nm, consistent with the (111) plane of face-centered cubic Ag. The enlarged TEM image of the region marked with red rectangle in Figure 2e is shown in Figure 2h. The EELS elemental images of this region are shown in Figures 2i–k, which clearly reveal a uniform distribution of Si and O in the CF region while Ag only concentrates in the nanoparticles region. These results further demonstrate that the CF is indeed composed of Ag nanocrystals.

To further clarify the dynamic growth of the Ag nanoparticle chain in the $Ag/SiO_2/Pt$ planar device, constant voltage stress (CVS) method was used to trigger the electroforming process and the SEM images on the different growth states of the Ag nanoparticle chain were captured at different CVS time, as shown in **Figure 3**. Firstly, the gap between electrodes of fresh device is clean, as shown in Figure 3a. After CVS (30 V, I_{CC}–10 μA) applied on Ag electrode for 10 s, some Ag nanoparticles are generated near Ag electrode, as shown in Figure 3b. After 150 s, more Ag nanoparticles are formed around Ag electrode and the nanoparticle chain extends towards Pt electrode, as shown in Figure 3c. Finally, a continuous Ag nanoparticle chain is formed and the device current reaches to the I_{CC} after CVS for 210 s due to the generation of more Ag nanoparticles and the further growth leading to their connection with each other, as shown in Figure 3d. The results clearly show that the initial Ag nanoparticle chain is firstly formed near the Ag anode and then gradually extends to the cathode, followed by the eventual formation of a whole nanoparticle chain between two electrodes. The similar growth process of the nanoparticle chain was also observed in other solid electrolyte systems.[17,21,32] Some previous studies reported that the TS phenomenon occurring in the CF-based RRAM is due to the spontaneously breaking of the thin CF induced by Joule heating effect.[23,33,34] However, in our work the SEM images visually demonstrate that the discrete Ag nanoparticle chain is originally generated during the electroforming process rather than developed from the thermal breaking of a continuous thin CF, indicating that the TS phenomenon in our device is not dominated by CF thermal instability.

Taking into account the difference of the CF morphology, we suggest that the MS and TS modes may have different conduction mechanism in the two resistive states. In the MS mode, the *I–V* curve in LRS follows a linear Ohmic conduction (Supporting Information Figure S3), indicating that the current mainly transports through a metallic-like continuous conductive path.[35] On the contrary, the *I–V* curve in HRS shows a complex nonlinear characteristic (Supporting Information Figure S3), which may be caused by the conduction mechanisms in typical insulator. The fitting results imply that the MS is attributed to the formation/dissolution of the CF under SET/RESET operations.[35]

Different to the MS mode, the CF consists of physically isolated Ag nanoparticles in the TS mode, which is a typical multi-metal-island systems.[36–40] **Figure 4**a–c show that the schematic diagram for the cross-section of the $Ag/SiO_2/Pt$ planar structure with a Ag nanoparticle chain, and the corresponding energy diagram and equivalent circuit. As can be seen from Figure 2e,f, the space of adjacent Ag nanoparticles in the CF region ranges from 2 nm to 5 nm. Hence, the gap between each pair of adjacent Ag nanoparticles of CF can be seen as

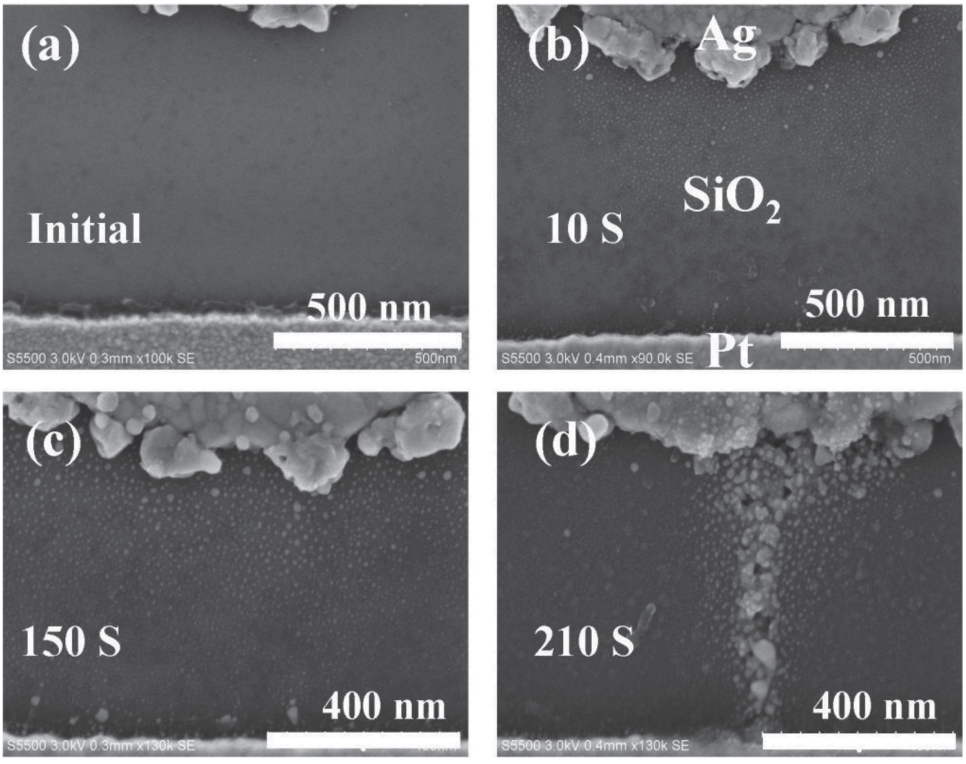

Figure 3. SEM images capturing the dynamic CF growth processes in the $Ag/SiO_2/Pt$ planar device. a) Fresh device. b–d) After 10 s, 150 s and 210 s under a 30 V constant voltage stress with I_{CC} = 10 μA, respectively.

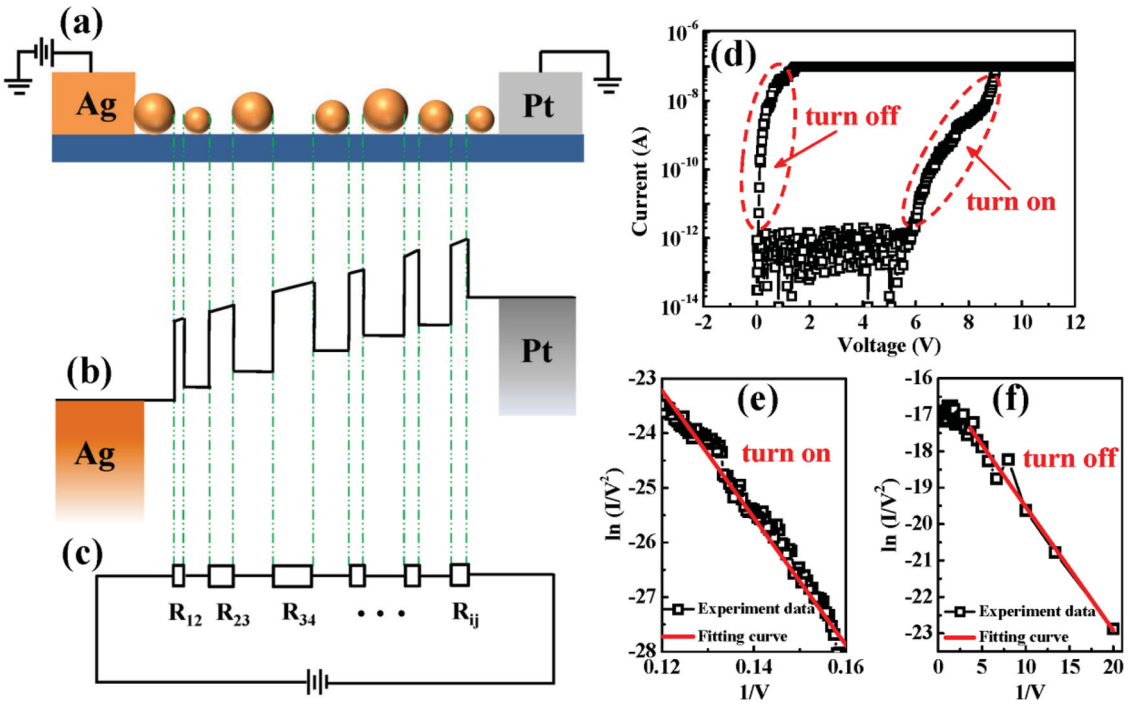

Figure 4. Schematic of CF consisting of isolated Ag nanoparticles and the corresponding energy diagram and current–voltage fitting characterization. a) Schematic cross-section of the Ag/SiO_2/Pt planar structure consisting of isolated Ag nanoparticles. b) The energy diagram corresponding to (a). c) The equivalent circuit model of (a). d) A typical *I*–*V* curve of the Ag/SiO_2/Pt planar device at TS mode. e,f) The $\ln(I/V^2)$ vs.$1/V$ curves replotted from the turn-on and turn-off regions in (d), respectively.

a tunneling junction and the charge carrier tunnels through these junctions when applying enough voltage between Ag and Pt electrodes, which is similar to the multi-metal-island systems.[36–38] Furthermore, the *I*–*V* fitting results further confirm that the tunneling transport mechanism dominates both turn-on (device switches from TS OFF-state to ON-state) and turn-off (device switches from TS ON-state to OFF-state) regions, as shown in Figure 4d–f. Figure 4d shows a typical *I*–*V* curve in TS mode, the turn-on and turn-off regions are marked by red dashed ellipse. Both turn-on and turn-off regions were redrawn into $\ln(I/V^2) - 1/V$ scale (Figure 4e,f). A clear linear relationship with negative slope is obtained in both regions, consistent with the feature of the tunneling mechanism.[40] It is worth noting that the similar fitting results are found in the Ag/SiO_2/Pt vertical device, as shown in Supporting Information Figure S4. From the equivalent circuit (Figure 4c), the total resistance (R) of the device is described as $R = \sum R_{ij} = V/I$. R_{ij} is defined as the tunneling resistance of the corresponding tunneling junction. As can be seen from Figure 4d, R obviously decreases when device switches from TS OFF-state to ON-state, indicating that the effective tunneling barriers of these junctions are reduced.[36,38]

To investigate the tunneling barrier change between TS ON-state and OFF-state, the potential profile along the nanocrystal chain was characterized in both states using KPFM. The schematic measurement of the KPFM is shown in the inset of **Figure 5**a. After electroforming with 50 nA, the *I*–*V* curve of a Ag/SiO_2/Pt planar device shows TS characteristic. Simultaneously, a clear nanocrystal chain is formed between Ag and Pt electrodes and its 2D topography by atomic force microscopic (AFM) measurement is shown in Figure 5b. The grain size of Ag nanocrystals varies from tens to hundreds of nanometers, and there are two large-size nanocrystal aggregations occurring in CF.

The electric potential distributions of the TS OFF-state and ON-state (respectively corresponding to the point a and b of TS curve in Figure 5a) were tested by KPFM. During KPFM measurement, a positive voltage is applied on the Ag electrode and the Pt electrode is grounded. For the TS OFF-state, the applied voltage increases from 0 V to 0.5 V and holds on 0.5 V, while for the TS ON-state, the voltage decreases from 9 V to 0.5 V and holds on 0.5 V. When the voltage is kept at 0.5 V, the KPFM tip scans the selected region and collects the corresponding potential data to draw the 2D electric potential distributions (Figures 5c-5d). The line profiles of potential in TS OFF-state and ON-state along or away from the Ag nanocrystal chain are extracted from the 2D potential distribution and redrawn in Figures 5e,f. To clearly show the discrepancy, the potential data are normalized in Figures 5e,f. In the TS OFF-state, the potential drop on SiO_2 layer is almost linear along the gap between two electrodes away from the nanocrystal chain (orange line in Figure 5e). However, in the potential distribution along the nanocrystal chain at OFF-state (black line in Figure 5e), there is an obvious potential jump between the two large nanocrystal aggregations. Different to the OFF-state, the potential drop on SiO_2 layer in the TS ON-state is almost the same along and away nanocrystal chain (Figure 5f). The potential jump between the nanocrystal aggregations is significantly reduced during the switching from the TS OFF-state to ON-state, implying that the resistance of the junction between the nanocrystal aggregation is greatly reduced. Therefore, the KPFM results confirm that

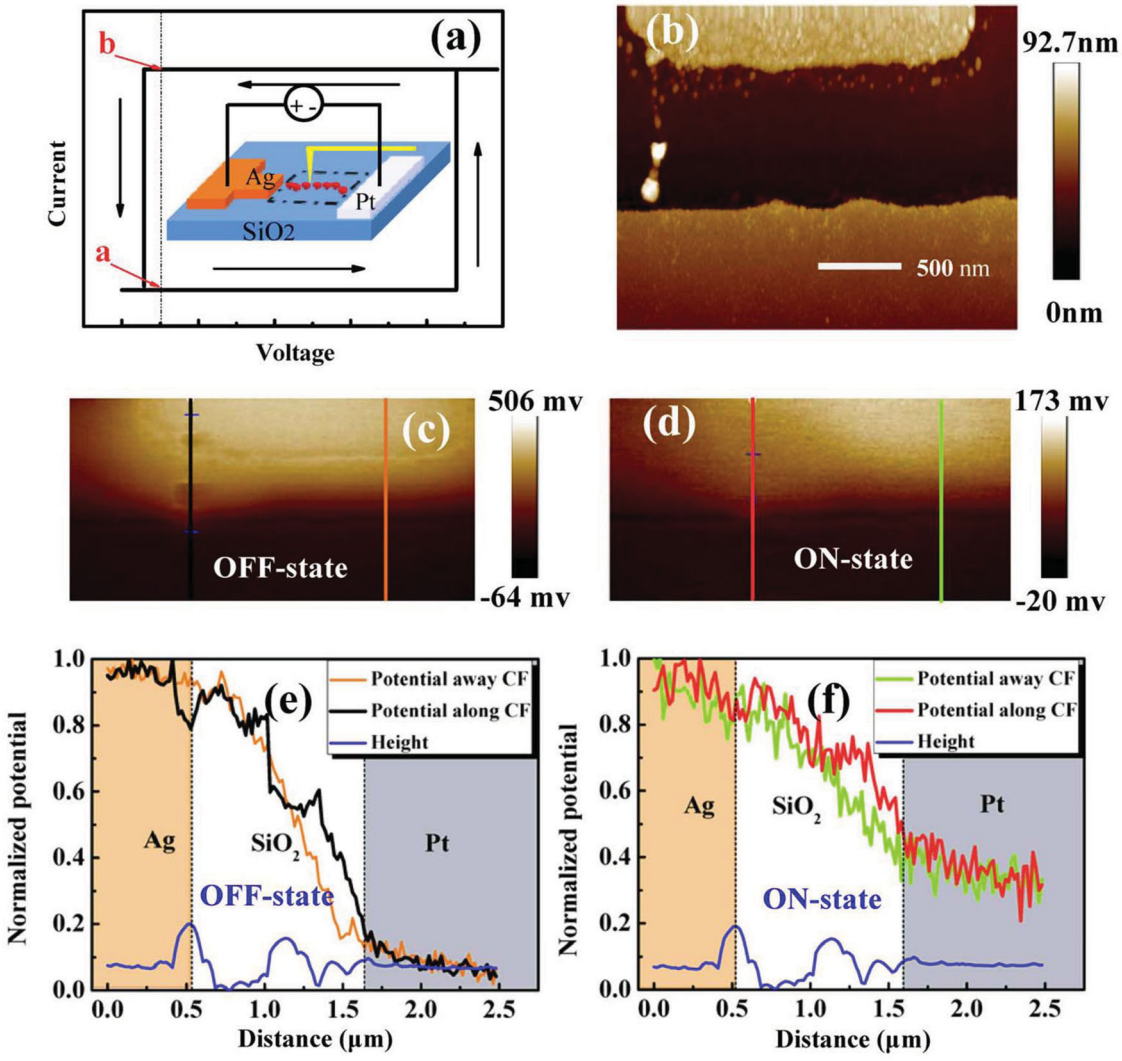

Figure 5. AFM and KPFM analysis results of a Ag/SiO_2/Pt planar device. a) Schematic of TS curve and the AFM measurement. Point a and b in the curve represents the TS OFF-state and ON-state of the device, respectively. b) The morphology of a CF between two electrodes. c,d) 2D potential distribution image in TS OFF-state and ON-state under 0.5 V voltage applied on Ag electrode, respectively. e) The potential distribution in TS OFF-state along (left black line in (c)) and away from (right orange line in (c)) the nanocrystal chain, respectively. f) The potential distribution in TS ON-state along (left red line in (d)) and away from (right cyan line in (d)) the nanocrystal chain, respectively. In (e,f), the blue lines are the topography of the SiO_2 surface along nanocrystal chain in (b).

the effective tunneling barrier (height and/or width) at TS ON-state is smaller than that at OFF-state. Based on the *I–V* fitting and KPFM results, the tunneling barrier modulation between discrete Ag nanocrystals should play an important role in the TS behavior. It is noted that many factors will induce the effective tunneling barrier modulation in this type of multi-metal-island system, such as ions migration between metal islands and/or charge trapping/detrapping in defects.[41] Further study is needed to identify the origin of the tunneling barrier modulation in the future.

3. Conclusion

In summary, we found that the TS and MS modes coexist in the Ag/SiO_2/Pt device. By increasing the I_{CC} in electroforming, the RS characteristics of the device transform from TS to MS mode. The SEM images prove that the RS characteristics are determined by the CF morphology. The TS and MS modes correspond to the CF consisting of isolated and continuous Ag nanocrystals, respectively. The SEM images of CF dynamic growth process show that the Ag nanoparticles are firstly formed near the Ag anode and then gradually grow to the cathode, which directly prove that the discrete Ag nanoparticle chain is originally generated during electroforming process rather than evolved from a continuous CF. Furthermore, the *I–V* fitting and KPFM characterization results imply that the tunneling barrier modulation between discrete Ag nanocrystals dominates the TS behavior. In the present work, the underlying nature of the TS and MS behaviors and the conversion between them are completely understood from the microcosmic point of view, which provides a guide to

control the two switching behaviors and to improve the device performances.

4. Experimental Section

Device Fabrication: For the Ag/SiO_2/Pt planar devices, a ≈100 nm thick SiO_2 layer was prepared on the Si substrate through thermal oxidation. After first photolithography, a ≈10 nm thick Ti adhesive layer and ≈70 nm thick Pt layer were deposited on the SiO_2 film by e-beam evaporation. Then, rectangle Pt electrode with area of 50 μm × 5 mm was released using a lift-off process. Subsequently, Ag electrode patterns composed of a 100 μm × 100 μm square and a 10 μm × 4 μm rectangle tip were generated by photolithography. Subsequently, 80-nm-thick Ag layer was deposited, and finally the Ag electrode was released by lift-off process. The length of the gap between Ag and Pt electrodes ranges from ≈100 nm to 2 μm. For the Ag/SiO_2/Pt vertical devices, a ≈70 nm thick SiO_2 film was deposited on a Pt/Ti/SiO_2/Si substrate by reactive rf sputtering, and then a ≈80 nm Ag film as top electrode was deposited by e-beam evaporation and patterned using photolithography. The device area is 100 × 100 μm^2.

Characterization: The electrical characterizations were performed in the atmosphere using semiconductor characterization system (Keithley_4200SCS). The morphology of CF in the device was detected using a field-emission scanning electron microscopic (Hitachi S4800). The crystalline structure and chemical composition of the CF was examined by a high-resolution transmission electron microscope (JEOL JEM2100F). The surface topography and potential was tested using atomic force microscopic (Bruker, Multimode 8).

Supporting Information

Supporting Information is available from the Wiley Online Library or from the author.

Acknowledgments

This work was funded by the Ministry of Science and Technology of China under grant Nos. 2010CB934200, 2011CBA00602, 2011AA010401 and 2011AA010402 and NSFC under grant nos. 61221004, 61106119, 61106082, 61334007, 61322408 and 61274091.

Received: April 23, 2014
Revised: May 22, 2014
Published online: July 14, 2014

[1] J. J. Yang, D. B. Strukov, D. R. Stewart, *Nat. Nanotechnol.* **2013**, *8*, 13.
[2] R. Waser, M. Aono, *Nat. Mater.* **2007**, *6*, 833.
[3] T. Hasegawa, K. Terabe, T. Tsuruoka, M. Anon, *Adv. Mater.* **2012**, *24*, 252.
[4] D. S. Jeong, R. Thomas, R. S. Katiyar, J. F. Scott, H. Kohlstedt, A. Petraru, C. S. Hwang, *Rep. Prog. Phys.* **2012**, *75*, 076502.
[5] H.-S. P. Wong, H.-Y. Lee, S. Yu, Y.-S. Chen, Y. Wu, P.-S. Chen, B. Lee, F. T. Chen, M.-J. Tsai, *Proc. IEEE* **2012**, *100*, 1951.
[6] M.-J. Lee, C. B. Lee, D. Lee, S. R. Lee, M. Chang, J. H. Hur, Y.-B. Kim, C.-J. Kim, D. H. Seo, S. Seo, U.-I. Chung, I.-K. Yoo, K. Kim, *Nat. Mater.* **2011**, *10*, 625.
[7] X. Zhu, W. Su, Y. Liu, B. Hu, L. Pan, W. Lu, J. Zhang, R.-W. Li, *Adv. Mater.* **2012**, *24*, 3941.
[8] J. J. Yang, M.-X. Zhang, J. P. Strachan, F. Miao, M. D. Pickett, R. D. Kelley, G. Medeiros-Ribeiro, R. S. Williams, *Appl. Phys. Lett.* **2010**, *97*, 232102.
[9] W. I. Park, J. M. Yoon, M. Park, J. Lee, S. K. Kim, J. W. Jeong, K. Kim, H. Y. Jeong, S. Jeon, K. S. No, J. Y. Lee, Y. S. Jung, *Nano Lett.* **2012**, *12*, 1235.
[10] Y.-E. Syu, T.-C. Chang, T.-M. Tsai, Y.-C. Hung, K.-C. Chang, M.-J. Tsai, M.-J. Kao, S. M. Sze, *IEEE Electron Device Lett.* **2011**, *32*, 545.
[11] Y. Li, H. Lv, Q. Liu, S. Long, M. Wang, H. Xie, K. Zhang, Z. Huo, M. Liu, *Nanoscale* **2013**, *5*, 4785.
[12] G. H. Kim, J. H. Lee, Y. Ahn, W. Jeon, S. J. Song, J. Y. Seok, J. H. Yoon, K. J. Yoon, T. J. Park, C. S. Hwang, *Adv. Funct. Mater.* **2013**, *23*, 1440.
[13] D.-H. Kwon, K. M. Kim, J. H. Jang, J. M. Jeon, M. H. Lee, G. H. Kim, X.-S. Li, G.-S. Park, B. Lee, S. Han, M. Kim, C. S. Hwang, *Nat. Nanotechnol.* **2010**, *5*, 148.
[14] F. Miao, J. P. Strachan, J. J. Yang, M.-X. Zhang, I. Goldfarb, A. C. Torrezan, P. Eschbach, R. D. Kelley, G. Medeiros-Ribeiro, R. S. Williams, *Adv. Mater.* **2011**, *23*, 5633.
[15] J.-Y. Chen, C.-L. Hsin, C.-W. Huang, C.-H. Chiu, Y.-T. Huang, S.-J. Lin, W.-W. Wu, L.-J. Chen, *Nano Lett.* **2013**, *13*, 3671.
[16] G.-S. Park, Y. B. Kim, S. Y. Park, X. S. Li, S. Heo, M.-J. Lee, M. Chang, J. H. Kwon, M. Kim, U.-I. Chung, R. Dittmann, R. Waser, K. Kim, *Nat. Commun.* **2013**, *4*, 2382.
[17] Q. Liu, J. Sun, H. Lv, S. Long, K. Yin, N. Wan, Y. Li, L. Sun, M. Liu, *Adv. Mater.* **2012**, *24*, 1844.
[18] Z. Xu, Y. Bando, W. Wang, X. Bai, G. Dmitri, *ACS Nano* **2010**, *4*, 2515.
[19] X. Zhu, C. S. Ong, X. Xu, B. Hu, J. Shang, H. Yang, S. Katlakunta, Y Liu, X. Chen, L Pan, J. Ding, R.-W. Li, *Sci. Rep.* **2013**, *3*, 1084.
[20] S. Peng, F. Zhuge, X. Chen, X. Zhu, B. Hu, L. Pan, B. Chen, R.-W. Li, *Appl. Phys. Lett.* **2012**, *100*, 072101.
[21] Y. C. Yang, P. Gao, S. Gaba, T. Chang, X. Pan, W. Lu, *Nat. Commun.* **2012**, *3*, 732.
[22] J. Sun, Q. Liu, H. Xie, X. Wu, F. Xu, T. Xu, S. Long, H. Lv, Y. Li, L. Sun, M. Liu, *Appl. Phys. Lett.* **2013**, *102*, 053502.
[23] S. H. Chang, J. S. Lee, S. C. Chae, S. B. Lee, C. Liu, B. Kahng, D.-W. Kim, T. W. Noh, *Phys. Rev. Lett.* **2009**, *102*, 026801.
[24] H. Y. Peng, Y. F. Li, W. N. Lin, Y. Z. Wang, X. Y. Gao, T. Wu, *Sci. Rep.* **2012**, *2*, 442.
[25] X. Saura, E. Miranda, D. Jiménez, S. Long, M. Liu, J. M. Rafí, F. Campabadal, J. Suñé, *Jpn. J. Appl. Phys.* **2013**, *52*, 04CD06.
[26] J. Qi, M. Olmedo, J.-G. Zheng, J. Liu, *Sci. Rep.* **2013**, *3*, 2405.
[27] Y.-J. Baek, Q. Hu, J. W. Yoo, Y. J. Choi, C. J. Kang, H. H. Lee, S.-H. Min, H.-M. Kim, K.-B. Kim, T.-S. Yoon, *Nanoscale* **2013**, *5*, 772.
[28] L. He, Z.-M. Liao, H.-C. Wu, X.-X. Tian, D.-S. Xu, G. L. W. Cross, G. S. Duesberg, I. V. Shvets, D.-P. Yu, *Nano Lett.* **2011**, *11*, 4601.
[29] S. H. Chang, S. B. Lee, D. Y. Jeon, S. J. Park, G. T. Kim, S. M. Yang, S. C. Chae, H. K. Yoo, B. S. Kang, M.-J. Lee, T. W. Noh, *Adv. Mater.* **2011**, *23*, 4063.
[30] X. Liu, S. M. Sadaf, M. Son, J. Park, J. Shin, W. Lee, K. Seo, D. Lee, H. Hwang, *IEEE Electron Device Lett.* **2012**, *33*, 236.
[31] H. Sun, H. Lv, Q. Liu, S. Long, M. Wang, H. Xie, X. Liu, X. Yang, J. Niu, M. Liu, *IEEE Electron Device Lett.* **2013**, *34*, 873.
[32] S. Gao, C. Song, C. Chen, F. Zeng, F. Pan, *Appl. Phys. Lett.* **2013**, *102*, 141606.
[33] C.-P. Hsiung, H.-W. Liao, J.-Y. Gan, T.-B. Wu, J.-C. Hwang, F. Chen, M.-J. Tsai, *ACS Nano.* **2010**, *4*, 5414.
[34] S. H. Chang, S. C. Chae, S. B. Lee, C. Liu, T. W. Noh, J. S. Lee, B. Kahng, J. H. Jang, M. Y. Kim, D.-W. Kim, C. U. Jung, *Appl. Phys. Lett.* **2008**, *92*, 183507.
[35] Q. Liu, S. Long, W. Wang, Q. Zuo, S. Zhang, J. Chen, M. Liu, *IEEE Electron Device Lett.* **2009**, *30*, 1335.

[36] C. H. Lee, S. Qin, M. A. Savaikar, J. Wang, B. Hao, D. Zhang, D. Banyai, J. A. Jaszczak, K. W. Clark, J.-C. Idrobo, A.-P. Li, Y. K. Yap, *Adv. Mater.* **2013**, *25*, 4544.
[37] A. Sattar, S. Fostner, S. A. Brown, *Phys. Rev. Lett.* **2013**, *111*, 136808.
[38] M. A. Savaikar, D. Banyai, P. L. Bergstrom, J. A. Jaszczak, *J. Appl. Phys.* **2013**, *114*, 114504.
[39] D. Xu, L. Qin, J. R. Heath, *Nat. Nanotechnol.* **2009**, *4*, 368.
[40] G. Dittmer, *Thin Solid Films* **1972**, *9*, 317.
[41] J. E. Morris, T. J. Coutts, *Thin Solid Films* **1977**, *47*, 3.